

Article

A New Insight into the Genesis of Graphite Deposits in Madagascar Using U–Pb Zircon Dating and Electron Microprobe Analysis

Ming-Jian Yang¹, Yong-Jun Di^{1,*}, Da Zhang^{1,*}, Da-Tian Wu^{1,2}, Ye Fang³ and Xin-Ming Zhang¹

¹ School of Earth Sciences and Resources, China University of Geosciences (Beijing), Beijing 100083, China; 13080203923@163.com (M.-J.Y.); wudatian@mail.cgs.gov.cn (D.-T.W.); 13701031529@163.com (X.-M.Z.)

² Nanjing Center, China Geological Survey, Nanjing 210016, China

³ Fujian Earthquake Agency, Fuzhou 350003, China; yefang2014@yeah.net

* Correspondence: diyongjun@cugb.edu.cn (Y.-J.D.); zhangda@cugb.edu.cn (D.Z.)

Abstract: Madagascar is globally recognized as an important producer of high-quality flaky graphite. However, current research on graphite deposits in Madagascar remains insufficient. Previous studies have linked the genesis of Madagascan graphite deposits to the metamorphism of sedimentary organic matter. Here, we provide a case study of graphite deposits in Madagascar, combining new data from the Ambahita graphite deposit (AMG) in southern Madagascar with data from the Antanisoa graphite deposit (ANG) in central Madagascar and the Vohitasara graphite deposit (VOG) on the east coast of Madagascar. We note that the mineral assemblages of graphite-bearing rocks in the AMG, ANG, and VOG are not typical of metamorphic mineral assemblages but rather the results of filling and metasomatism by mantle-derived fluids that occurred after peak metamorphism. Electron microprobe analysis indicates that the graphite of the AMG, VOG, and ANG is usually associated with phlogopite or Mg-biotite; the phlogopite shares a common genesis with other widespread phlogopite deposits across Madagascar. We reveal that the distribution of graphite deposits in Madagascar is primarily controlled by ductile shear zones between blocks. Ductile shear zones that extend deep into the mantle can provide an ideal migration channel and architecture for the emplacement of mantle-derived fluids. The graphite mineralization formed no earlier than the peak metamorphism (490 Ma) and no later than the intrusion of pegmatite veins (389 ± 5 Ma). The distribution of graphite deposits, graphite orebody morphologies, mineral associations, and geochemical data suggest that the genesis of graphite deposits in Madagascar is linked to mantle-derived fluid filling rather than the metamorphism of sediments, as previously suggested. These findings have important implications for similar deposits in Madagascar and potentially globally.

Keywords: U–Pb geochronology; electron microprobe analysis; mantle-derived fluid filling; graphite deposit; Madagascar



Citation: Yang, M.-J.; Di, Y.-J.; Zhang, D.; Wu, D.-T.; Fang, Y.; Zhang, X.-M. A New Insight into the Genesis of Graphite Deposits in Madagascar Using U–Pb Zircon Dating and Electron Microprobe Analysis. *Minerals* **2024**, *14*, 484. <https://doi.org/10.3390/min14050484>

Academic Editors: Zhenyu Chen, Fangyue Wang and Yuri N. Palyanov

Received: 24 March 2024

Revised: 24 April 2024

Accepted: 29 April 2024

Published: 2 May 2024



Copyright: © 2024 by the authors. Licensee MDPI, Basel, Switzerland. This article is an open access article distributed under the terms and conditions of the Creative Commons Attribution (CC BY) license (<https://creativecommons.org/licenses/by/4.0/>).

1. Introduction

With the emergence of new materials and energy production methods, graphite and its derivatives have become crucial in electronics, national defense, aerospace, and the nuclear industry [1–7]. Moreover, graphite serves as a crucial catalyst in facilitating metal formation [8,9]. The straightforward classification of graphite generally relies on size, structure, and mode of occurrence, categorized as lumpy (coarse crystals), flaky (crystalline), and amorphous (cryptocrystalline < 70 μm) [10,11]. Among these, flaky graphite stands out for its favorable physicochemical properties, extensive applications, and high industrial value [12]. Madagascar has been acknowledged as a prominent producer and exporter of graphite, particularly large flaky graphite, since the early 20th century [13–16], producing up to 200 million tons, as of 2022. Madagascar boasts proven graphite ore reserves of 30 million tons and total resources reaching up to 200 million tons [17]. Nonetheless,

research on graphite deposits in Madagascar, particularly concerning their genesis, remains limited. The genesis of graphite deposits is often defined using carbon isotope data. Predominantly, graphite deposits in Madagascar are believed to have originated from sediment metamorphism, as indicated by their light carbon isotopic compositions [18–20]. While some researchers propose the transformation of organic matter into graphite occurs via prograde metamorphism (graphitization) [21,22], others argue for the derivation of graphite from inorganic sources such as carbonates [23,24]. Yang et al. [25] reported the existence of inorganic carbon in the Antanisoa graphite deposit (ANG) and suggested that carbon isotope exchange between organic and inorganic carbon occurred during the formation process.

The question of whether the graphite is of organic or inorganic origin has been debated for many years, with two main genetic models being proposed: growth during metamorphic processes, or precipitation from fluids or melts [26–30]. The $\delta^{13}\text{C}$ values of mantle-derived rocks, such as kimberlites and carbonatites, lie between -2% and -9% [31–33]. However, lighter carbon isotopic compositions of up to -26% have been recently reported from mantle diamonds and graphite [34]. A growing number of researchers in recent years have shown that graphite can form through the deposition of solid carbon from C–O–H fluids derived from sub-lithospheric sources [11,35–37]. Touzain et al. [38] confirmed a magmatic origin for vein graphite deposits from the Bogala and Kahatagaha–Kolongaha mines in Sri Lanka based on the physical and chemical attributes of the graphite. Zhang and Santosh [39] investigated the Kerala graphite deposit in southern India and reported that the graphite $\delta^{13}\text{C}$ values had two distinct origins: the relatively lighter values represented a mixture of biogenic and magmatic carbon, whereas the heavier values represented graphite precipitation from CO_2 -rich fluids from sub-crustal magmatic sources. Similarly, Yang et al. [25] argued that the primary origin of a graphite deposit in central Madagascar was mantle-derived fluid filling rather than metamorphism of sediments, as previously suggested. In 1963, Craig showed that the isotopic composition of a graphite sample is rarely a valid indicator of its origin, because inorganic carbon can also have light carbon isotopic compositions, for example, olivine basalt, andesite, and trachyte of the Hawaiian Islands have $\delta^{13}\text{C}$ values of -25.4% , -24.8% , and -19.0% , respectively [40]. Hence, more attention should be paid to the petrographic and mineralogical characteristics and mineral assemblages within graphite deposits; these can provide more comprehensive evidence of the genesis of graphite deposits in Madagascar, rather than relying solely on carbon isotope data.

Graphite deposits are widespread throughout Madagascar. We chose three typical graphite deposits from eastern, central, and southern Madagascar for field investigation. In our previous study, we examined the geological characteristics of the ANG from the Antananarivo block, central Madagascar [25], and the Vohitasara graphite deposit (VOG) located on the eastern coast of Madagascar [41]. In this study, we investigated the geological characteristics and origin of the Ambahita graphite deposit (AMG) in southern Madagascar using a combination of petrography, mineralogy, zircon U–Pb dating, and electron microprobe analysis. We then synthetically analyzed the graphite distribution characteristics of the three aforementioned graphite deposits. Our results provide a deeper understanding of the mineralization process of these graphite deposits and propose a new theory for discussing the genesis of coeval graphite deposits elsewhere in Madagascar.

2. Regional Geological Setting

Madagascar is an island off the east coast of Africa, separated from the African continent by the Mozambique Channel. It has experienced a complex tectonic evolution since the Archean, including the formation of an Archean–Paleoproterozoic paleo-continental basement, Mesoproterozoic paleo-continent breakup, subduction of oceanic crust, and continental collisional orogeny. This has created a diverse range of sedimentary formations, magmatic events, and post-metamorphic deformation styles, resulting in favorable geological conditions for various types of mineralization [42,43].

As a region with a widespread distribution of ancient basement, Madagascar shows a close relationship between its multi-stage formation and evolution from the Precambrian to early Paleozoic. The Precambrian crystalline basement distributed across central and eastern Madagascar is considered to have been part of the Dharwar craton [44]. The Antongil block (Figure 1), the oldest of the basement units, located in the central–eastern domain of Madagascar, primarily consists of Mesoarchean metamorphosed sedimentary rocks of greenschist and amphibolite facies, as well as Neoproterozoic metamorphosed granites and mafic schists. Three greenstone belts composed of mafic gneiss and schist are also important components of the craton in the Antananarivo block [45]. Therefore, the formation and evolution of the Precambrian crystalline basement in Madagascar are closely related to the formation of the ancient continental nucleus of the Dharwar craton and continental accretion during the Meso–Neoproterozoic. During the Neoproterozoic, Madagascar developed extensive basic–acid volcanic and intrusive rock suites, such as the Neoproterozoic Imoroma–Itsindro suite that overlies Archean greenschists in the Antananarivo block. This was associated with some rift sedimentation, suggesting that Madagascar may have been an important component in the breakup of Rodinia during the Neoproterozoic [46]. After the breakup of Rodinia, Madagascar entered into the assembly and orogenic phases of Gondwanaland during the Neoproterozoic and Early Paleozoic [47]. The tectonic evolution of Madagascar has left behind significant evidence, with the formation of numerous accretionary blocks, tectonic suture zones, and magmatic and metamorphic events [48]. In northern Madagascar, the Bemarivo block was accreted over the Antongil block via thrusting along the Sandrakota shear zone. Similarly, in southern Madagascar, the Vohibory terrain collaged along the Ranotsara shear zone on the western side of the Androyen and Anosyen blocks [48,49]. Ampanihy, extending over 200 km and exhibiting sinistral features, is an important NNE-trending ductile shear zone in the region, traversing the Androyen unit (Figure 1). Many graphite deposits of different scales are distributed across this region. Tight and synclinal folds formed within the shear zone owing to compression and shearing action. There are also a number of small occurrences of medium–acidic labradorite distributed as lenses along the trend of this zone.

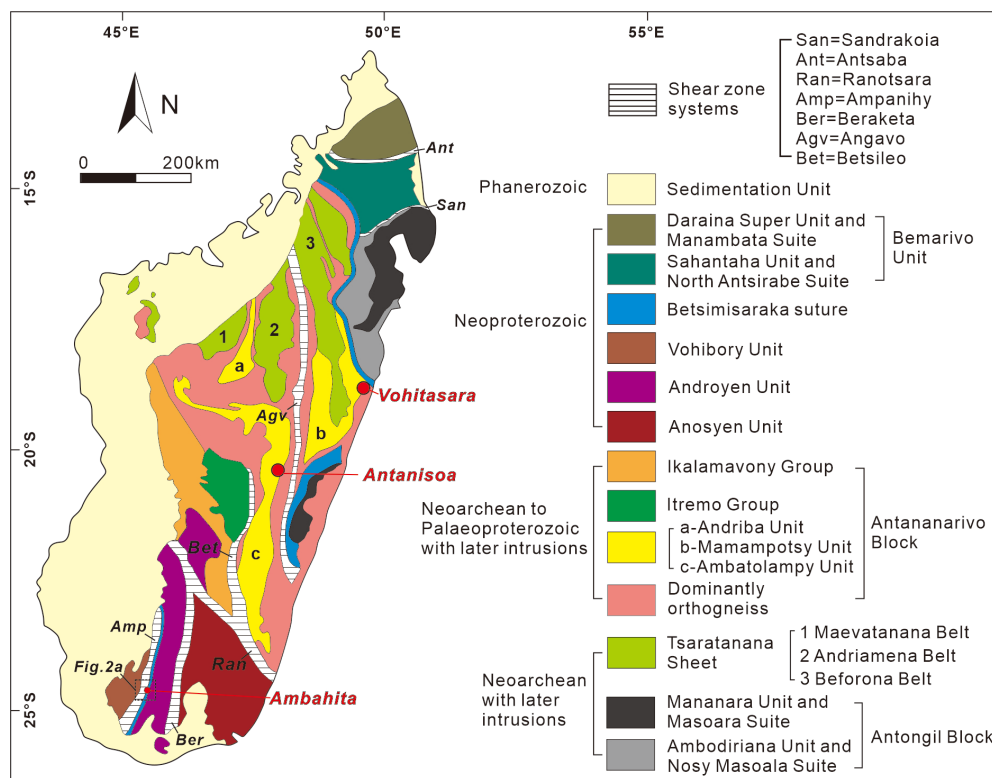


Figure 1. Tectonic division of Madagascar (after [48,49]).

The AMG, located in the Androyen block, is situated in the Bekily region of southern Tulear Province, Madagascar (Figure 2a). From west to east, the Precambrian metamorphic crystalline basement strata exposed in the domain are the Late Archean Androyen Group, Graphite Group, and Early Paleoproterozoic Vohibory Group [50]. These groups are easily identifiable in the field because of their component lithologies [51,52]. The Androyen Group, which mainly consists of mafic garnet-bearing granofels, is located in the eastern part of the AMG and trends north–south. The Graphite Group, located in the central–western part of the AMG and widening from south to north, forms a large graphite mineralization belt trending NNE with a width of 3–28 km and length of >200 km. The main lithologies of this group are garnet-bearing granofels and graphite-bearing granofels, with the latter forming the principal ore-hosting strata of the graphite deposit. The Vohibory Group, which mainly comprises granofels, amphibolite gneiss, and amphibolite, is located in the western part of the AMG.

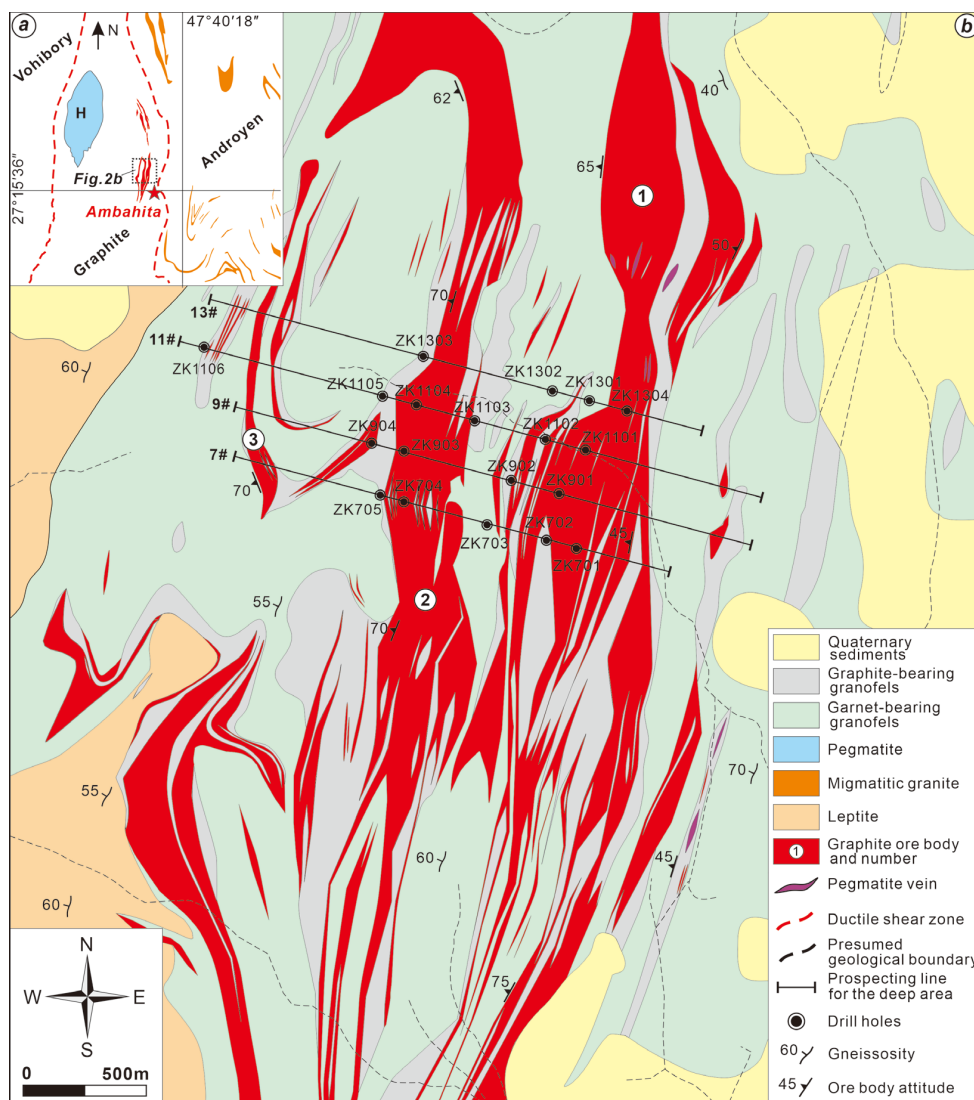


Figure 2. (a) Simplified regional geological map of the Ambahita ore district in southern Madagascar. (b) Simplified geological map of the Ambahita graphite deposit. Modified from [53].

The regional tectonics are characterized by a ductile shear zone, with various types of folds. The dominant magmatic rock is pegmatite, which contains enstatite and is primarily distributed in the northwest AMG as a small pluton with a length of ca. 15 km and width of ca. 6 km [53]. The pluton displays an “eyeball-shaped” north–south trend. Furthermore,

a variety of migmatitic granites occur in the Androyen Group, which have widths ranging from 200 to 2000 m and lengths ranging from 2 to 10 km (Figure 2a).

3. Geology of the AMG

3.1. Field Relationships and Ore Body Description

The exposed strata in the AMG are the Late Archean Graphite Group, which includes leptyte, garnet-bearing granofels, and graphite-bearing granofels, displaying a clear-cut lithological sequence (Figure 2b). Leptyte is mainly found in the western part of the district, and it has a light gray color (lighter than granofels), fine-grained blastic texture, and massive structure. It comprises approximately 65% plagioclase, 30% quartz, and minor amounts of biotite and graphite, with dark-colored minerals making up approximately 5% of the total. Garnet-bearing granofels is widely distributed across the AMG (Figure 2b), displaying a gray color, medium-fine-grained blastic texture, and weak-gneissic or massive structure. It comprises 40%–50% feldspar, 20%–30% quartz, 10%–20% garnet, and minor amounts of dark-colored minerals such as biotite. Graphite-bearing granofels crops out in the mid-eastern part of the AMG (Figure 2b) and is the main host rock for the graphite orebodies. It exhibits a distinct gray to dark gray color, flaky fine-grained texture, and gneissic to weak gneissic structure. It comprises feldspar (40%–60%), quartz (20%–30%), graphite (1%–10%), and minor amounts of biotite. Additionally, Quaternary sediments, with a thickness of 0–4 m, are widely distributed across the AMG.

A total of 12 orebodies have been identified in the AMG, overall occurring in a stratiform-like manner, among which orebodies No. 1 and No. 2 are the largest and most important (Figures 2b and 3). Orebody No. 1 is located in the central-eastern part of the ore district, measuring 6100 m in length and 120.8–327.4 m in thickness. The fixed carbon grade ranges from 2.66% to 9.02%, with an average of 4.25%. The southern part of orebody No. 1 extends from north to south, while the northern part is aligned in a NNE direction. Orebody No. 2 is located to the west of No. 1; it is 5880 m in length and 99.5–198.9 m in thickness, with a fixed carbon grade ranging from 2.83% to 8.82% (average 5.81%). Meanwhile, orebody No. 3, which is located in the western part of the ore district, has a length of 2355 m and a thickness ranging from 12.5 to 133.0 m, with a fixed carbon grade of 3.46% to 6.87% (average 4.72%). The strike and dip angles of orebodies No. 1 and No. 2 are similar at 260–295° and 45–50°, respectively, whereas orebody No. 3 strikes at 245–300° and dips at 70–75° (Figure 3).

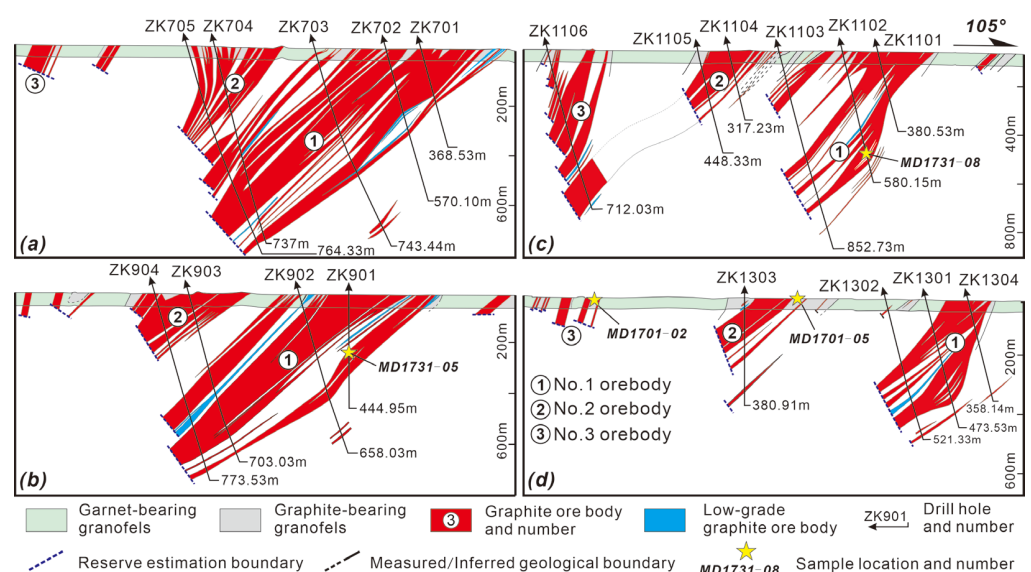


Figure 3. Cross-section of the AMG, including the No. 7 exploration line (a); No. 9 exploration line (b); No. 11 exploration line (c); and No. 13 exploration line (d) (modified from [53]).

The exploration trench of line 13, a key observation site with a 110° bearing, is bounded by graphite-bearing granofels to the east and non-graphite-bearing gneiss to the west. This exploration trench mainly contains graphite-bearing granofels and garnet-bearing granofels (Figure 4a). According to surface exploration and drill-hole data, there is no graphite mineralization in the garnet-bearing granofels, which likely comprises the hanging-wall and foot-wall of the graphite ore body between orebodies No. 2 and No. 3 (Figure 3). Graphite orebodies are mainly hosted in the graphite-bearing granofels (Figure 4b,c), occurring as either veins following the gneissosity trend and dipping to the northwest (Figure 4d) or fillings within gneiss as flaky aggregates (Figure 4e). The breakstones of quartz veins (Figure 4f) and Fe–Mn mineralization (Figure 4g) are seen on the surface along the exploration trench, indicating intense fluid activity. There is no significant graphite mineralization in the western part of the trench. Meanwhile, gneissosity folding in the graphite-bearing granofels indicates that the western part of the trench is more significantly affected by shearing (Figure 4h). The appearance of pegmatite veins around the exploration trench is associated with a pronounced increase in graphite enrichment around the veins, reflecting the process of graphite activation and re-enrichment during fracture-filling mineralization (Figure 4i).

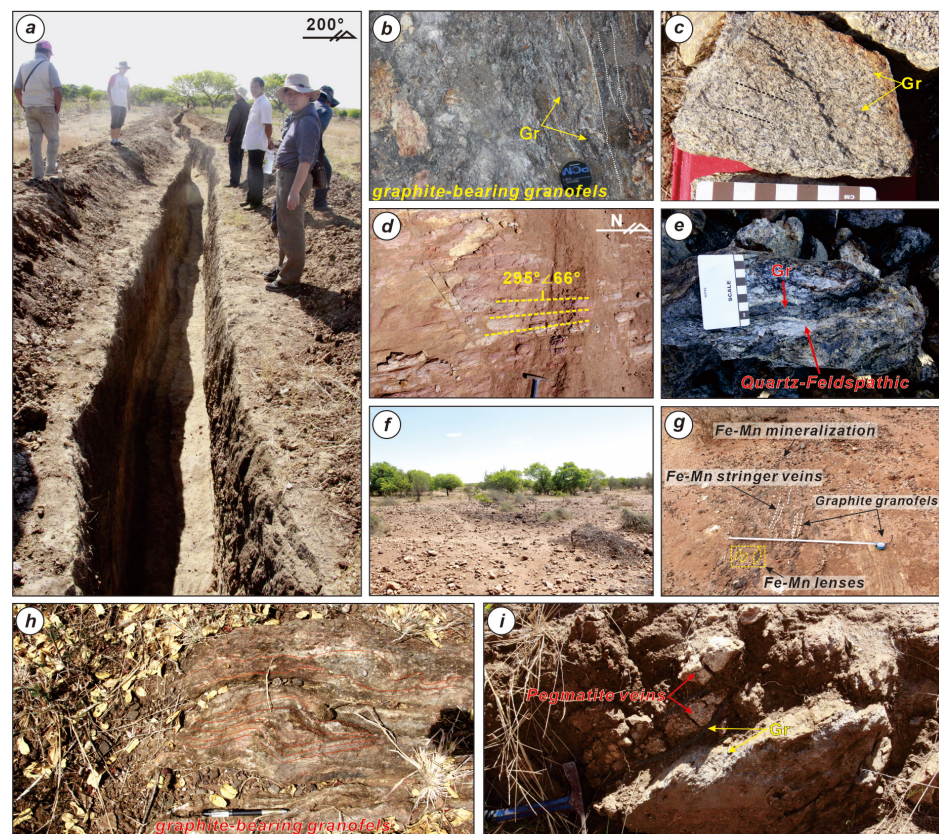


Figure 4. Field photographs of the AMG. (a) The exploration trench of the No. 13 exploration line. (b) Graphite orebodies developed along the gneissosity in graphite-bearing granofels. (c) Graphite orebodies developed along the schistosity of graphite-bearing granofels. (d) Veined graphite orebodies developed along the gneissosity in the central part of the exploratory trench. (e) Flaky graphite with lepidoblastic texture, filling along the gneissosity in graphite-bearing granofels. The graphite orebodies in the felsic component are barren. (f) The breakstones of quartz veins on the surface. (g) Fe–Mn mineralization occurring as veins or lenses along the schistosity of graphite granofels in the eastern part of the exploratory trench. The yellow dotted box indicates lenses of Fe–Mn mineralization. The white dashed lines indicate Fe–Mn stringer veins. (h) The gneissosity of the graphite-bearing granofels is folded in the western part of the exploratory trench. (i) The enlargement and enrichment of the graphite flakes around the edges of pegmatite veins.

3.2. Petrographic Description

The ore mineral of the AMG is graphite, while gangue minerals mainly include quartz, feldspar, and mica. There are two types of mica: yellowish-brown biotite and light-yellow or nearly colorless phlogopite with weak polychromatism (Figure 5a,b). Under a reflected light microscope, graphite is brownish-gray in color, has a lepidoblastic texture, and has a particle size of 0.04–2 mm (Figure 5c). It shows good directionality and fills between quartz and feldspar grains (Figure 5d). Graphite and mica are symbiotic, filling each other along their cleavage planes (Figure 5e). These flaky graphite and mica minerals are aggregated, thickened, and oriented, forming gneissic and veined structures owing to the strong ductile shear of the graphite-bearing granofels. There is a small amount of graphite filling in garnet-bearing granofels near the graphite ore bodies. The garnets have developed fractures as a result of shear damage, which are now filled with flaky graphite (Figure 5f). Some quartz in the garnet-bearing granofels is enclosed in garnet grains that are cut by graphite (Figure 5g). Melt droplets of graphite and biotite are included in quartz grains (Figure 5h). Similarly, numerous melt droplets of quartz and graphite are developed in dravite in the ANG (Figure 5i).

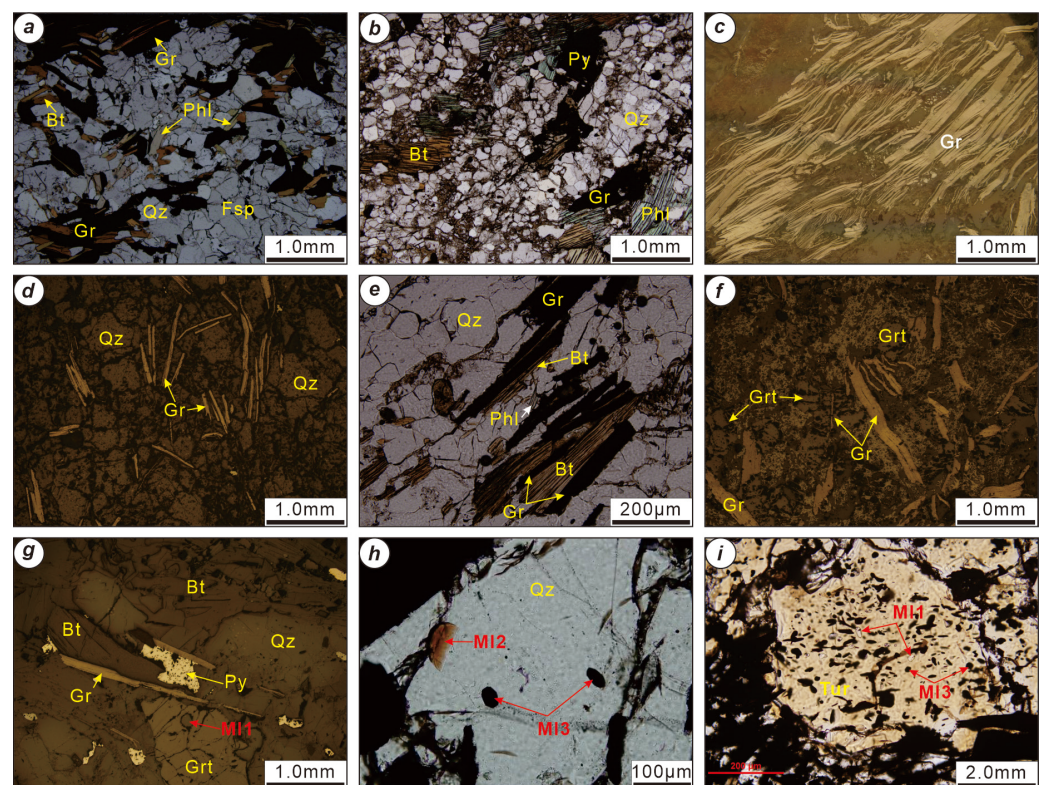


Figure 5. Representative photomicrographs of minerals from the AMG. (a) Biotite and phlogopite intergrown with graphite (plane-polarized light). (b) Serpentine alteration occurring in phlogopite (plane-polarized light). (c) Oriented flaky graphite (reflected light). (d) Flaky graphite filling between quartz and feldspar grains and along their cracks (reflected light). (e) Graphite and biotite filling each other along cleavage planes (plane-polarized light). (f) Flaky graphite filling garnet fractures (reflected light). (g) Graphite intergrown with euhedral quartz and biotite, filling their fractures. The garnet grain includes quartz melt inclusions (reflected light). (h) Quartz grain with graphite and biotite melt inclusions (cross-polarized light). (i) Tourmaline in graphite schist from the ANG containing melt droplets of graphite and silicate minerals (plane-polarized light).

4. Sampling and Analytical Methods

4.1. Sampling

In this study, four samples of micas related to graphite mineralization were selected from drill holes in the AMG. Sample MD1731-05 was obtained from the ZK901 drill hole at a depth of 230 m (Figure 3b); sample MD1731-08 was obtained from the ZK1102 drill hole at a depth of 444 m (Figure 3c); and samples MD1701-02 and MD1701-05 were obtained from the vicinity of the graphite orebody of exploration line 13 (Figure 3d). In addition, two samples (201A and TT1-1-b) were obtained from the soil surface near the graphite orebody in the VOG. Polished thin sections were made from all samples for petrographic observation and electron microprobe analysis.

A total of nine samples were selected from the ANG, AMG, and VOG for U–Pb zircon geochronological analysis. These comprised three samples (102, 103A, and 110B) of graphite schist from the ANG, two samples (201A and 202D) of graphite schist and two samples (201C and 201D) of quartz veins from the VOG, and two samples of pegmatite from the ANG (101A) and VOG (202C), respectively.

4.2. Electron Microprobe Analysis

Major and minor element contents were determined using a JEOL JXA-8230 electron microprobe at the electron probe laboratory of the Regional Geological and Mineral Resources Survey Institute, Hebei, China. Peak counting times were set to 10 s for all major elements and 20 s for all minor elements. Analyses were performed with an accelerating voltage of 15 kV, probe current of 20 nA, and 5 µm beam diameter for all elements. The laboratory standards were quartz (Si), plagioclase (Al), rutile (Ti), almandine (Fe), rhodonite (Mn), forsterite (Mg), calcite (Ca), albite (Na), and sanidine (K). The analytical error for major oxides was approximately 1%. The method used was the Electron Probe Quantitative Analysis Method specified in General Rule: GB/T 15074-2008.

4.3. Zircon U–Pb Analysis

Zircon grains were first separated from the MD1705-1 sample using conventional heavy liquid and magnetic separation techniques combined with hand picking. The zircon separates, together with grains of the zircon standard [54], were then mounted in epoxy. Subsequently, all zircon grains on the mounts were documented using transmitted light, reflected light, and cathodoluminescence (CL) images to decode their external and internal structures.

Zircon U–Pb analyses were undertaken using laser ablation–inductively coupled plasma–mass spectrometry (LA–ICP–MS; Agilent 7500a) by Kecui Testing Technology Co., Ltd., Beijing, China, using a NWR193 laser denudation system and a Jena PQMS ICP–MS. The experimental data were processed using Glitter 4.0 software. Owing to the small amount of ^{207}Pb present in young zircons, which results in low count rates and high analytical uncertainties, the $^{206}\text{Pb}/^{238}\text{U}$ ratios are generally considered to be the most reliable data for concordant Phanerozoic zircons [55]. Ordinary Pb was corrected using the 3D coordinate method. Uncertainties in the weighted-mean ages are quoted at $\pm 1\sigma$, which is at the 95% confidence level. Isoplot 4.15 was used for the age calculations.

5. Results

5.1. Electron Microprobe Analysis of Biotite

We performed six electron probe point analyses on the MD1731-08 sample, five on the MD1701-02 sample, eleven on the MD1731-5 sample, and seven on the MD1701-5 sample from the AMG. Similarly, we performed six electron probe point analyses on the 201A sample and thirteen on the TT1-1-b sample from the VOG. The structural formula of biotite was calculated using Minpet 2.02 mineralogical data processing software, based on 22 oxygen atoms (Supplementary Table S1). The SiO_2 contents in MD1731-5 and MD1701-5 ranged from 40.33% to 47.06% (average 43.49%) and from 40.50% to 47.77% (average 45.38%), respectively; these values were markedly higher than those in MD1731-8

and MD1701-2. Compared with MD1731-8 and MD1701-2, the biotite in MD1731-5 and MD1701-5 had higher Al_2O_3 and lower FeO and MgO . However, all of these samples had negligible Na_2O and CaO contents and subtle variations in K_2O , similar to samples from the ANG in central Madagascar [25].

In the VOG samples, a minor occurrence of reddish-brown biotite was observed under the optical microscope in both 201A and TT1-1-b. Some biotite had evidently undergone alteration during subsequent stages, displaying heightened fracturing. Notably, the SiO_2 (39.71%–41.18%) and K_2O (9.03%–11.0%) contents in sample TT1-1-b were higher than those in sample 201A (31.94%–39.18% and 4.76%–9.74%, respectively). Conversely, the FeO contents were markedly lower in the former (1.61%–2.15%) compared with those in the latter (10.55%–14.31%).

In an $\text{Mg-Fe}^{3+} + \text{Al}^{\text{VI}} + \text{Ti-Fe}^{2+} + \text{Mn}$ mica classification diagram, all the points analyzed in sample 201A and some of the points analyzed in sample MD1731-8 plot in the Mg-biotite field (Figure 6). All points analyzed in samples TT1-1-b and MD1701-2 plot in the phlogopite field, as do those from sample 110-1 from the ANG. In addition, some of the points analyzed in samples 1731-5 and 1701-5 plot in the phlogopite field, whereas others plot in the muscovite field (Figure 6). The $\text{Fe}^{2+}/(\text{Mg} + \text{Fe}^{2+})$ ratios in both the AMG and the VOG range from 0.01 to 0.43, with relatively constant values (Supplementary Table S1), indicating that the micas have not undergone markedly late-stage hydrothermal alteration [56]; this is consistent with the optical microscope observations but inconsistent with the ratios observed in the ANG.

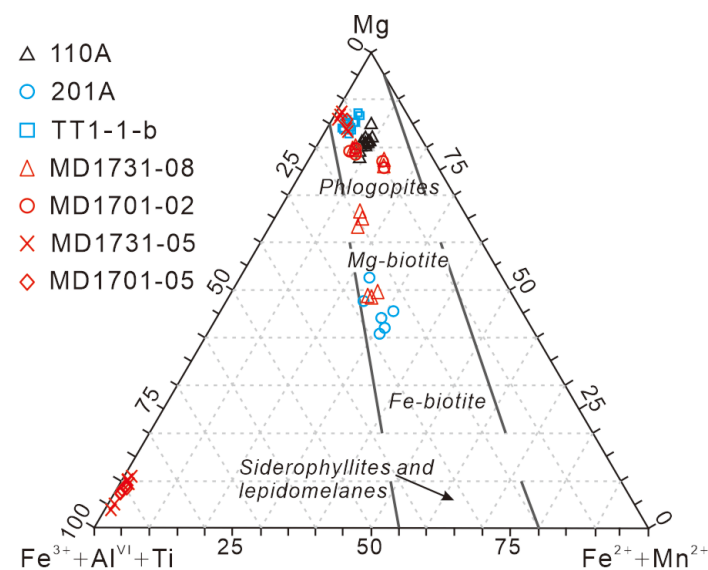


Figure 6. $(\text{Al}^{\text{IV}} + \text{Fe}^{3+} + \text{Ti-Fe}^{2+} + \text{Mn}^{2+}\text{-Mg})$ ternary classification of micas from the AMG, VOG, and ANG in Madagascar (after [57]). Note: Red for AMG; Blue for VOG; Black for ANG (data are from [25]).

5.2. Zircon $U\text{-Pb}$ Ages

5.2.1. Zircons in Graphite Schists

Zircon grains in graphite schists (102, 103A, and 110B) from the ANG were mainly colorless to pale brown, euhedral–subhedral in shape, ranged from 20 to 125 μm in length, and had length-to-width ratios ranging from 1:1 to 2:1. In CL images, they showed evident regular oscillatory zoning typical of magmatic zircons. A few zircon grains had dark accretionary edges ($<10\ \mu\text{m}$), which may be the result of recrystallization caused by later metamorphism.

Zircon grains from the three samples varied markedly with respect to their U (86–3810 ppm) and Th (26–562 ppm) contents, and their Th/U mass ratios varied from 0.01 to 1.47. Thirty-one valid data points were obtained from these three samples, all of which showed good concordance (Figure 7a). The zircons had an age spectrum ranging

from 2551 to 218 Ma and were mainly distributed in the ranges of 2551–1716 Ma (12 data points), 1096–919 Ma (3 data points), and 578–218 Ma (16 data points) (Supplementary Table S2). The apparent age at point nine of sample 102 was 239 ± 4 Ma; this was the youngest age obtained from a magmatic zircon from graphite schists within the ANG. The youngest $^{206}\text{U}/^{238}\text{Pb}$ age of a zircon from sample 103A was 218 ± 4 Ma; this grain showed the characteristics of a metamorphic zircon. Zircons from sample 110B had $^{206}\text{Pb}/^{238}\text{U}$ ages ranging from 578 to 490 Ma; according to the CL images, most of these were metamorphic zircons.

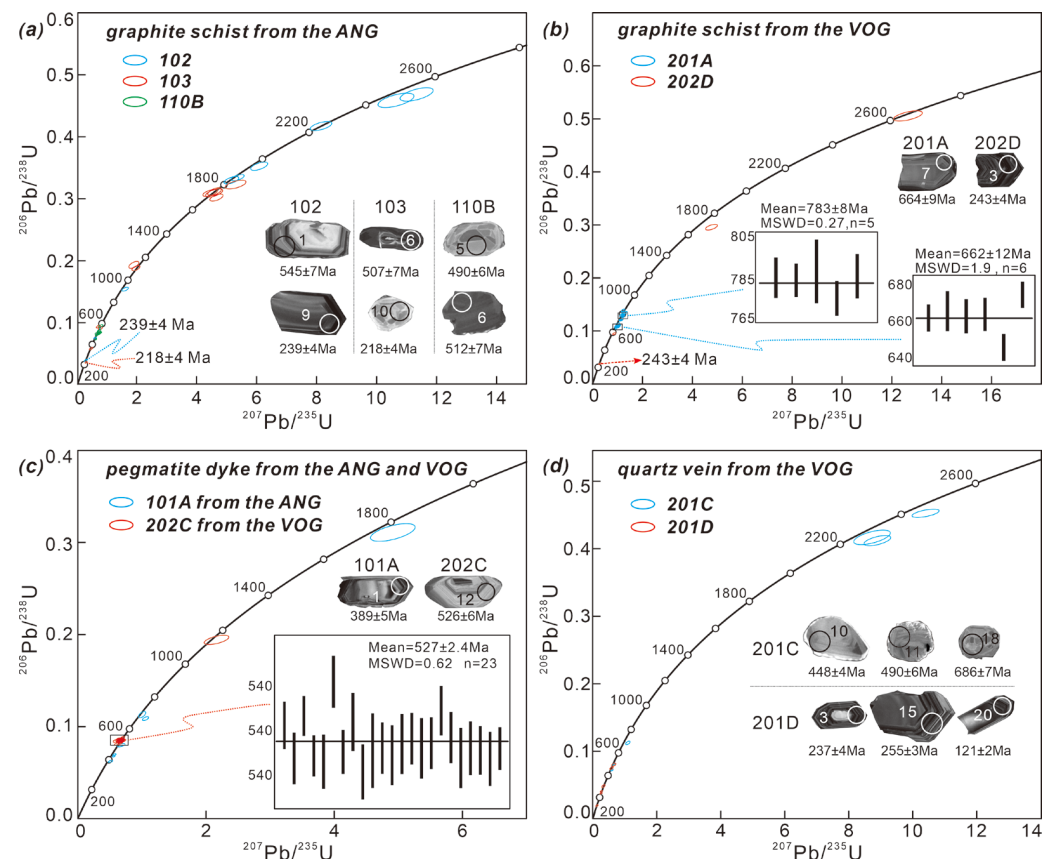


Figure 7. Representative CL images and LA-ICP-MS zircon U-Pb concordia plots of graphite schist from the ANG (a) and VOG (b), pegmatite veins from the ANG and VOG (c), and a quartz vein from the VOG (d). Error ellipses are 1σ . The insets indicate the weighted mean $^{206}\text{Pb}/^{238}\text{U}$ ages.

The characteristics of zircons in samples 201A and 202D were similar to those of the three samples described above. They had variable concentrations of U (231–2505 ppm) and Th (20–630 ppm). Their Th/U mass ratios varied from 0.02 to 0.79, with an average value of 0.30, reflecting the characteristics of magmatic zircons [58]. Most of the age data from sample 201A showed good concordance (Supplementary Table S3), with three main groupings of 833–813 Ma, 787–734 Ma (mean = 783 ± 8 Ma), and 691–644 Ma (mean = 662 ± 12 Ma) (Figure 7b). In addition to the above age ranges, apparent ages of 2638 ± 27 and 1665 ± 18 Ma were also obtained from sample 202D; the youngest zircon age in sample 202D was 243 ± 4 Ma (Figure 7b).

5.2.2. Zircons in Pegmatite Veins

Zircons from sample 101A, a tourmaline-bearing pegmatite vein from the ANG, had subhedral to euhedral shapes and ranged from 40 to 100 μm in length, with length-to-width ratios ranging from 1:1 to 2:1. Their CL images showed concentric oscillatory zoning with low to variable luminescence, indicative of a magmatic origin. The U and Th contents and Th/U mass ratios of this sample are shown in Supplementary Table S4. Seven valid data points were obtained, among which the youngest age was 389 ± 5 Ma.

Zircons grains from sample 202C, a plagiopegmatite vein from the VOG, ranged in length from 20 to 100 μm , with aspect ratios of 1:1 to 2:1. Most grains had a subhedral to euhedral shape, exhibiting good oscillatory zoning in CL images. Their U and Th contents varied from 89 to 1455 ppm and from 67 to 251 ppm, respectively. Their Th/U mass ratios varied from 0.15 to 0.75, with a median value of 0.16 (Supplementary Table S4), indicative of a magmatic origin [58]. A total of 28 concordant to near-concordant analyses produced $^{207}\text{Pb}/^{206}\text{Pb}$ ages between 547 ± 6 and 502 ± 5 Ma, except for one analysis that gave a much older age of 1144 ± 18 Ma. Twenty-three analyses of sample 202C produced a weighted-mean $^{206}\text{Pb}/^{238}\text{U}$ age of 527 ± 2.4 Ma ($n = 23$, MSWD = 0.62) (Figure 7c).

5.2.3. Zircons in Quartz Veins

Zircons from sample 201C, a quartz vein from the VOG, ranged in length from 25 to 100 μm , with aspect ratios of 1:1 to 2:1. Their CL images revealed a variety of internal textures: no zoning, patchy zoning, and weak oscillatory zoning. Among a total of six analyses (from six separate zircon grains), the Th/U mass ratios varied from 0.02 to 11.78, with a median value of 0.7 (Supplementary Table S5), indicative of a magmatic origin [58]. Three zircon grains showed metamorphic characteristics, with $^{206}\text{Pb}/^{238}\text{U}$ ages of 686 ± 7 , 490 ± 6 , and 448 ± 4 Ma, respectively (Figure 7d).

Zircon grains from sample 201D were up to 120 μm in length, with aspect ratios of 1:1 to 2:1. Most grains were predominantly euhedral to subhedral and exhibited oscillatory zoning in CL images (Figure 7d). Some grains had dark cores with light-gray overgrowths. Six spot analyses were performed on six zircons (Supplementary Table S5). The dated zircons had U and Th contents of 92–1083 and 38–3759 ppm, respectively, with Th/U mass ratios of 0.17–3.47 (median value of 0.57), indicative of a magmatic origin [58]. Six zircon grains in sample 201D with apparent ages of 495 ± 9 , 468 ± 7 , 303 ± 5 , 255 ± 3 , 237 ± 4 , and 121 ± 2 Ma showed clear regular oscillatory zoning in CL images, typical of magmatic zircons (Figure 7d).

6. Discussion

6.1. Previous Views of the Genesis of Graphite Deposits

Graphite deposits are widely thought to result from either the conversion of carbonaceous matter through regional or contact metamorphism or from deposition from carbon-bearing fluids [10]. The former processes result in syngenetic deposits of either amorphous or flaky graphite, depending on the metamorphic grade of the host rock [59]. Flaky graphite usually occurs in high-grade gneisses, quartzites, or granulite facies rocks. The latter process forms epigenetic vein deposits, in which lumpy graphite occurs.

Winchell [60] suggested that seams of graphite that are strictly parallel to bedding in marbleized limestone and quartz schist potentially result from the metamorphism of carbonaceous layers present in such rocks. Metamorphism of such carbonaceous layers usually results in the production of so-called “amorphous” graphite, which is very fine-grained and usually impure. However, it seems probable that more intense metamorphism would produce purer and coarser graphite.

Fluid-deposited graphite displaying high crystallinity was previously thought to be restricted to high-temperature environments (mainly granulite facies terranes). However, large concentrations of highly crystalline graphite can also precipitate from moderate-temperature fluids [35]. In veined graphite deposits associated with magmatism, during the main stage of graphite formation, graphitization can be achieved via the following

reactions: $\text{CO}_2 \rightarrow \text{C} + \text{O}_2$ [61]; $\text{CH}_4 + \text{O}_2 \rightarrow \text{C} + 2\text{H}_2\text{O}$ [62]; $\text{CO}_2 + \text{CH}_4 \rightarrow 2\text{C} + 2\text{H}_2\text{O}$ [62]; and $2\text{CO} \rightarrow \text{C} + \text{CO}_2$ [63]. Each of these reactions happens under specific conditions, and the focus is on the state and solubility of CO_2 in magma. Lowenstern [64] reported that the solubility of CO_2 in mantle melt/magma is solely dependent on pressure and oxygen fugacity. Carbon distribution in the mantle may be highly heterogeneous, including the possibility of massive carbon enrichments on a local scale, particularly in the shallow sub-continental mantle [65]. Graphite was reported from dolomite carbonatite at Pogranichnoe, Russia, which also has mantle carbon isotope signatures [66]. Rajesh et al. [67] believe that the C responsible for the formation of graphite in dolomite carbonatite was in the form of CO_2 in the source melts and the crystallization of graphite occurred by C saturation under a reducing environment and continued until it reached a higher oxidation state, and they consider that sulfides present in the rock acted as a reducing agent that resulted in the precipitation of graphite from a CO_2 medium. Palyanov et al. [68], on the basis of experimental data and thermodynamic calculations, revealed the role of sulfides as a reducing agent for CO_2 fluid, regardless of its solid or melt state. Although significant carbonate minerals have not been observed in the AMG, ANG, or VOG in Madagascar to date, previous studies suggested that graphite can precipitate in the mantle under specific physicochemical conditions. Moreover, Dienes et al. [34] revealed that lighter carbon isotopes from mantle diamonds and graphite had a composition of up to -26% , indicating that carbon in the mantle could exist in the form of substance carbon, not just as CO_2 or CH_4 . The mantle-derived carbon probably serves as a primary source for the graphite in most graphite deposits in Madagascar. As for the lighter carbon isotopes in the mantle, some proposed that the role of carbon recycling into the mantle was the possible cause [34], although this is a subject of debate. The precipitation mechanism of C is beyond the scope of this paper.

6.2. Distribution and Mineralization of Graphite Deposits in Madagascar

The distribution of graphite deposits in Madagascar is mainly controlled by ductile shear zones between blocks. The main ore-bearing units are the Antananarivo block and its contact margins with other blocks, especially the Itremo group, Tsaratanana sheet, Betsimisaraka block, and Ampanihy shear zone between the Androyen and Vohibory blocks (Figures 1 and 8). A small number of graphite deposits have also been found near the ductile shear zone; for example, in the Sahantaha block, North Antsirabe suite, and Archean migmatite gneisses [69]. The distribution of graphite deposits and extensive graphite mineralization across multiple tectonic units constrain the genesis and mineralization of the graphite deposits. Metamorphism of sediments cannot account for the widespread distribution of graphite mineralization in multiple tectonic units that were not originally joined. There are two possible explanations for this phenomenon. Firstly, the sedimentation of organic matter may have occurred before the convergence of different tectonic units in Madagascar, and the organic matter was transformed into graphite deposits through metamorphism. However, this explanation falls short of adequately accounting for the fact that graphite deposits are mainly developed along the ductile shear zones (Figure 9). Secondly, a unified process of mineralization might have occurred after the separate tectonic units were assembled; this appears to be a more plausible possibility, whereby the ductile shear zone reaching deep into the mantle provided a potential migration channel and ore-bearing space for deep carbonic fluids (probably carbon and other carbon-bearing, mantle-derived, fluid-rich melts [70]).

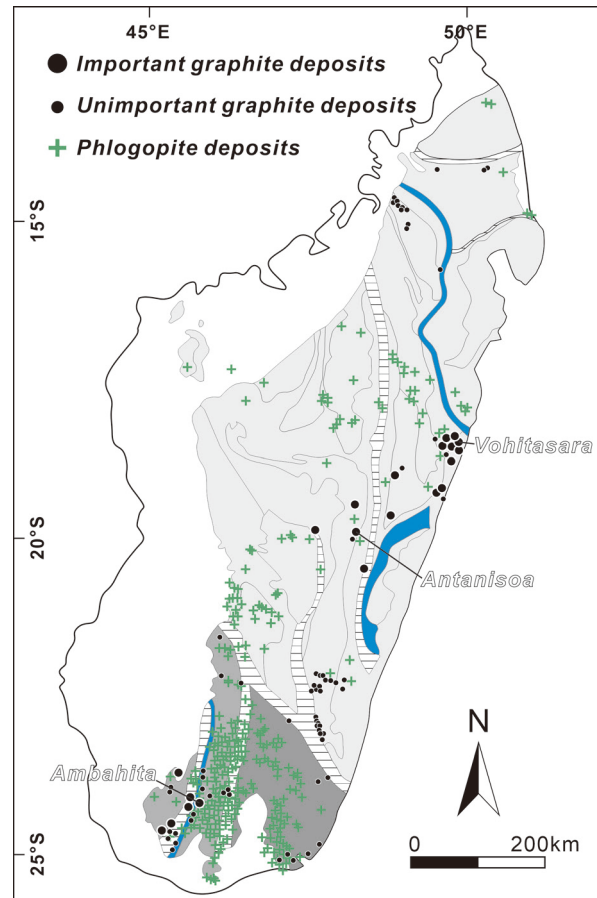


Figure 8. Distribution map of graphite and phlogopite deposits in Madagascar (after [48,71]).

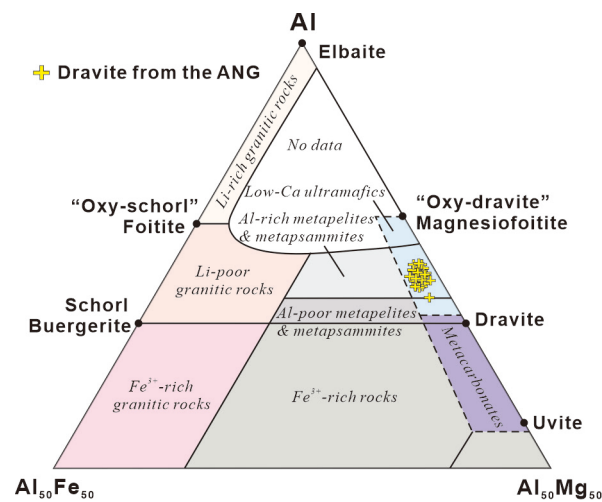


Figure 9. Al-Al₅₀Fe₅₀-Al₅₀Mg₅₀ diagram (base map modified after [72]; data from [25]).

6.3. Melt Inclusions and Mineral Assemblages

Tourmaline, a mineral often overlooked in petrological studies, has been shown to be a useful petrogenetic indicator mineral [72–74]. Two kinds of tourmalines, black and light yellow, were found in ANG. The light-yellow tourmaline was dravite with a high magnesium content, as identified by electron microprobe analysis (Supplementary Table S6). Notably, there are melt inclusions of graphite, quartz, and K-feldspar in light-colored dravite within graphite schists from the ANG (Figure 5i) [25]. There are two possible explanations for this phenomenon. Firstly, the dravite may have formed at peak

metamorphism and includes the residues of graphite, quartz, and K-feldspar. Secondly, the dravite may have formed via the crystallization of magma rich in volatiles. Dravite is associated with phlogopite in the same sample from the ANG, indicating that the magnesium may have been supplied by dolomitic marble in the region, or by ultramafic magma. In an Al^{IV} - Fe^{2+} - Al_50Mg_50 diagram, all the points analyzed in the dravite plot in the low-Ca meta-ultramafics field (Figure 9). The dravite in the ANG indicates that the magnesium probably originated from ultramafic rocks [25].

In an Al^{IV} versus $Fe^{2+}/(Fe^{2+} + Mg)$ diagram, micas from the AMG, VOG, and ANG demonstrate an Mg-rich nature (Figure 10a). In an $FeO^T/(FeO^T + MgO)$ versus MgO diagram, most micas plot in the phlogopite field and others plot in the Mg-biotite field, indicating a dominantly mantle source region, with some mixing of crustal material (Figure 10b).

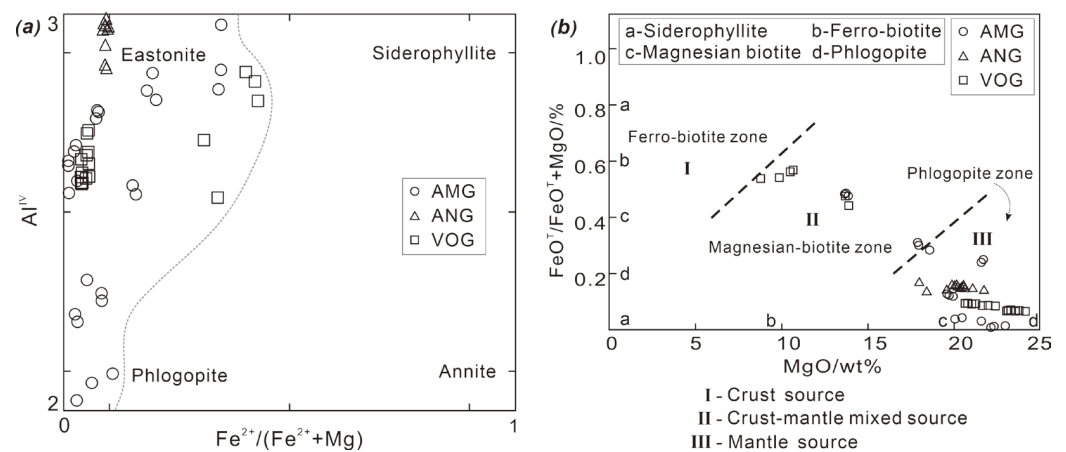


Figure 10. Compositions of micas from the AMG, VOG, and ANG on (a) Al^{IV} - $Fe^{2+}/(Fe^{2+} + Mg)$ and (b) $FeO^T/(FeO^T + MgO)$ -MgO diagrams ((a) after [75]; (b) after [76]).

The VOG, ANG, and AMG contain veined graphite deposits, suggesting a process of carbon activation, migration, and reprecipitation. The minerals associated with graphite in graphite schists from the VOG and ANG are quartz, phlogopite, Mg-biotite, and dravite [25,41]. Iron-bearing minerals infilled the cleavage cracks in graphite during a later period, which may have been contemporaneous with the iron mineralization and iron veins filling gneiss outside the AMG. The minerals associated with graphite in the AMG are quartz, feldspar, phlogopite, Mg-biotite, and pyrite. Evidently, pyrite infilled the graphite cleavage cracks at a later stage. There are plagiopegmatite intrusions in the AMG, characterized by pronounced sericitization of plagioclase. Additionally, there is a small amount of graphite present in quartz veins that are filled along fractures. Meanwhile, there are also plagiopegmatite veins in the VOG, including plagioclase with extensive argillization. Plagiopegmatite and quartz veins are present across all three ore districts, with a small quantity of graphite observed in these veins; the size of graphite flakes tends to increase at the edges of the veins [25,41].

The difference in mineral assemblages between the graphite schists and graphite-bearing granofels suggests a greater possibility of fluid filling rather than equilibrium metamorphic mineral assemblages; this is also supported by the several periods of vein formation mentioned above. Graphite-bearing granofels are the main ore-hosting rocks in the AMG, whereas the hanging-wall and footwall are mainly composed of garnet-bearing granofels lacking graphite mineralization or with only a small amount of graphite occurring along their edges. The mineral assemblages in the garnet-bearing granofels, including garnet, plagioclase, K-feldspar, biotite, and quartz, conform more closely to an equilibrium metamorphic mineral assemblage. One possibility is that the garnet-bearing granofels are the products of peak metamorphism, while the graphite ore bodies filled the structural fractures of the garnet-bearing granofels later. The distribution of graphite orebodies shown in Figure 2 also demonstrates clear characteristics of fluid filling along structural fractures.

6.4. Mantle-Rooted Shear Zones in Madagascar as Channels of Mantle-Derived Fluids

Graphite-bearing rocks are widespread in southern Madagascar and are spatially associated with major near-vertical shear zones that have been interpreted to be rooted in and controlled by the mantle [77]. Previous researchers divided the crust in this area into three zones: outside of shear zones, minor shear zones, and major shear zones. This division was based on three independent data sets: field and satellite mapping [78,79]; C-, H-, and O-isotope geochemistry [80,81]; and gravimetry [82]. Mantle-derived CO₂ was tapped, showing carbon fluxes of the same order of magnitude as oceanic ridge degassing [83]. One major shear zone shows abundant phlogopite—diopside—apatite—calcite mineralization (a well-known paragenesis of mantle metasomatism) owing to mantle-fluid infiltration and its interaction with the crust. Carbonatitic magmas possibly collected in the major shear zones at the base of the crust and may have provided the source for CO₂ upwellings as well as other metasomatic agents. Small-scale minor shear zones were controlled by crustal deformation processes and the crust-derived H₂O-rich fluids. Widespread fluid circulation was limited to the vicinity of syn-metamorphic plutons [77], with fluid-absent conditions dominating elsewhere. Mantle-CO₂ flushing is not required for granulite genesis but is a consequence of high associated heat flux [77]. Fluid transfer at the mantle/crust interface is controlled by the tectonic setting and associated geothermal gradient. Moreover, Pili et al. [77] demonstrated the existence of metasomatized lithospheric shear zones that provide channels for the movement of mantle volatiles. Such metasomatism is responsible for the formation of the main phlogopite deposits in Madagascar.

The distribution of phlogopite deposits in Madagascar is generally similar to that of graphite deposits, commonly occurring near the contacts of different tectonic units. The southern part of Madagascar hosts the largest number of these deposits (Figure 9; [48,71,84]). The graphite deposits investigated herein are characterized by phlogopite and Mg-biotite associated with graphite, suggesting a possible genetic relationship between the formation of these graphite deposits and the major phlogopite deposits in Madagascar. Ramambazafy et al. [85] showed that fluid inclusions in different minerals from gneisses and skarns in southeastern Madagascar are CO₂-rich. They also demonstrated that equilibrium occurred between granulite mineral paragenesis and a CO₂-rich fluid phase, indicating that the formation of graphite deposits in this region likely originated from the metamorphism of granulite. Furthermore, Rajesh et al. [67] reported on the origin of graphite in glimmerite and spinellite from an ultramafic complex in the Achankovil shear zone in southern India; on the basis of carbon isotopes, they believed that the graphite was typical of mantle-derived graphite, and hydration reactions (the removal of water from the system) leading to phlogopite crystallization was a factor controlling graphite precipitation.

6.5. Timing of Formation of Graphite Deposits in Madagascar

The late Neoproterozoic to Cambrian history of East Africa is characterized by two major thermal events. The periods from approximately 750 to 620 Ma [69,70,86,87] and 580 to 510 Ma [88,89] are thought to relate to the closure of the Mozambique Ocean, resulting in the amalgamation of Gondwanaland. There are contrasting opinions as to which period represents the final closure of the ocean. One model suggests that early closure occurred by 620 Ma as a result of the collision between “African” cratons and other fragments. In this model, tectonism between 580 and 510 Ma is deemed to be post-collision related, reflecting orogenic collapse [90,91]. Conversely, a second model proposes that the final closure did not occur until approximately 550 Ma [91,92]. In this model, tectonism predating 620 Ma is attributed to early accretion of continental fragments or magmatic underplating.

Hulscher and Fitzsimons [93] suggested that tectonism between 580 and 510 Ma was largely driven by extension in the early closure model based on patterns of tectonic deformation at approximately 550 Ma observed in central Madagascar, whereas convergence-related shortening predominated in the model for final amalgamation at approximately 550 Ma; this is consistent with age determinations for the Angavo shear zone [69,86,92]. At approximately 540 Ma, deformation in the cover was dominated by sinistral transpression, which

continued until approximately 530 Ma, when lateral escape could no longer be accommodated. Therefore, Central Madagascar provides evidence for continued convergence, rather than a post-collisional extensional setting between 550 and 530 Ma. Although the work of Hulscher and Fitzsimons [93] supports the model proposing the later second stage closure of the Mozambique Ocean, it does not rule out the possibility of a multi-phase assembly, which could have involved the accretion of continental fragments other than Madagascar to East Africa by 620 Ma.

The apparent ages of graphite schists from the VOG and ANG are 358 ± 5 , 243 ± 4 , and 239 ± 4 Ma (Figure 7a,b). The presence of zircons, derived from either magma or magma-related fluids, suggests a contribution of Hercynian and Indosinian magmatism or superposition of ore-forming materials during mineralization. The apparent ages of graphite schists from the ANG with good concordance are 833 ± 12 to 813 ± 8 , 789 ± 14 to 734 ± 8 , and 691 ± 9 to 644 ± 7 Ma (Figure 7a), indicating the ages of the source region(s) of the graphite schists. Thus, the sedimentary age of the Ambatolampy Group in the ANG cannot be earlier than the Cryogenian period of the Neoproterozoic; in other words, the timing of formation of the ANG cannot be earlier than the Cryogenian.

Pegmatite veins emplaced into graphite schists of the ANG yielded concordant apparent ages of 1745 ± 31 , 690 ± 13 , 664 ± 8 , 494 ± 7 , 433 ± 4 , 423 ± 4 , and 389 ± 5 Ma (Figure 7c). All of these, except for 389 ± 5 Ma, represent the ages of magmatic zircons captured during the intrusion of the pegmatite veins. The apparent age of 389 ± 5 Ma may represent the crystallization age of the pegmatite or the earliest date of intrusion of the pegmatite.

The timing of peak metamorphism in Madagascar has been inferred to be in the range of 600–500 Ma [94–100]. The mineral assemblages of the three graphite deposits described above show that they were not affected by peak metamorphism, suggesting that the formation time of graphite deposits in Madagascar was after 500 Ma. A metamorphic zircon from a quartz vein yielded a concordant apparent age of 490 ± 6 Ma (Figure 7d); this zircon probably formed during peak metamorphism and was recrystallized by later fluids, based on the loss of uranium at the edge of the zircon.

Martin et al. [84] obtained the timing of phlogopite mineralization (approximately 490 Ma) using Rb and Sr isotope data from the Sakavary and Sakamasy deposits in the Beraketa and Tranomaro belts, respectively; these data are consistent with phlogopite K/Ar ages (485 and 491 Ma) from Ampandrandava analyzed by Rakotondrazafy et al. [101]. A further analysis of phlogopite from Ampandrandava, using the more robust $^{40}\text{Ar}/^{39}\text{Ar}$ method, gave an age of 481 ± 2 Ma (Archibald, Queen's University). As mentioned earlier, phlogopite is closely associated with graphite in the study area, suggesting that the formation age of the graphite deposits is similar to that of the phlogopite deposits. Therefore, the fluid that recrystallized the aforementioned metamorphic zircon is likely closely related to that which formed the graphite deposits. In summary, the formation age of the graphite deposits was likely no earlier than 490 Ma and no later than the intrusion of the pegmatite veins (389 Ma).

Furthermore, magmatic zircons from a quartz vein of the VOG yielded concordant apparent ages of 303 ± 5 , 255 ± 3 , 237 ± 4 , and 121 ± 2 Ma (Figure 7d). Among these, 121 ± 2 Ma potentially represents the age of quartz vein formation, or at least suggests that the formation of quartz veins occurred no earlier than the Early Cretaceous. Meanwhile, the other apparent ages younger than 389 Ma show that there were periods of magmatic activity in the Late Carboniferous, Late Permian, and Triassic, which may have played important roles in the enrichment of graphite deposits in this area.

In summary, most of the graphite deposits in Madagascar are distributed along the ductile shear zones (Figure 8). Therein, phlogopite and/or Mg-biotite are commonly intergrown with graphite assemblages. Commonly, these graphite deposits are adjacent to the phlogopite deposits near ductile shear zones, especially in southern Madagascar (Figure 9), and they were possibly both formed after peak metamorphism, implying a genetic relationship between the formation of these graphite deposits and phlogopite

deposits in Madagascar. As discussed above, drop-shaped graphite melt inclusions in quartz (Figure 5h) and dravite suggest a possible origin of graphite from mantle fluids. Ductile shear zones that extend deep into the mantle can provide ideal migration channels and ore-bearing space for mantle-derived fluids (Figure 11). We propose that mantle-derived fluids upwelled and brought up the carbon and magnesium to the shallow crust, then formed the graphite deposits (Figure 11).

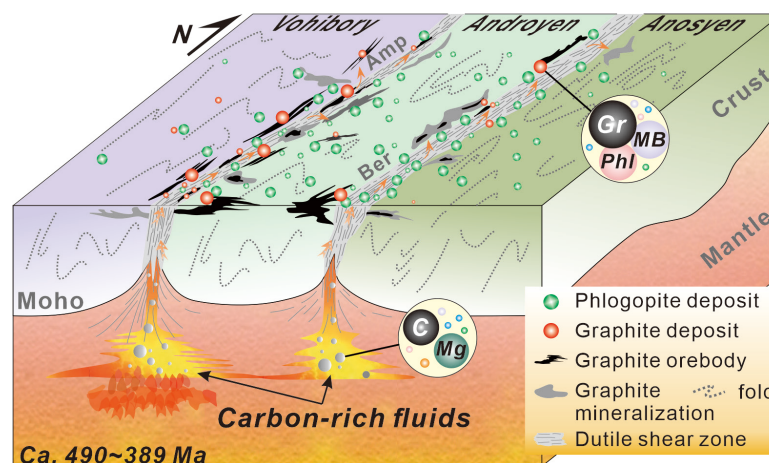


Figure 11. Preliminary schematic diagram showing the graphite deposits linked to mantle-derived fluid filling in Madagascar (base map from [78]). Abbreviations: Amp—Ampanihy, Ber—Beraketa, Gr—Graphite, Phl—Phlogopite, MB—Magnesian biotite.

7. Conclusions

We investigated mineral assemblages, electron microprobe analysis, and U–Pb zircon ages of the ANG, AMG, and VOG to discuss the genesis of graphite deposits and constrain the approximate age of graphite mineralization in Madagascar. Our main conclusions are as follows.

1. We reveal that graphite of the AMG in Madagascar is usually associated with phlogopite and Mg-biotite; this is consistent with the mode of graphite occurrence in the ANG in central Madagascar and the VOG on the east coast of Madagascar. The formation of the aforementioned minerals was likely facilitated by the addition of external material and fluids. It is possible that the phlogopite in these deposits shares a common genesis with widespread phlogopite deposits elsewhere in Madagascar, and the magnesium was perhaps derived from the mantle.
2. We note that the paragenetic associations of minerals associated with graphite in the AMG, ANG, and VOG are not metamorphic mineral assemblages in character; instead, they are the results of fluid filling after peak metamorphism. The genesis of these three graphite deposits may be closely related to the circulation of mantle-derived fluids.
3. The graphite mineralization ages in the AMG, ANG, and VOG were no earlier than the timing of peak metamorphism (490 Ma) and no later than the intrusion of pegmatite veins at 389 ± 5 Ma, as constrained by zircon U–Pb geochronology.

Supplementary Materials: The following supporting information can be downloaded at: <https://www.mdpi.com/article/10.3390/min14050484/s1>, Table S1: Representative electron-microprobe analyses of micas at the AMG, VOG, and ANG, Madagascar. Table S2: U–Pb isotope data of zircons of graphite schist from the ANG. Table S3: U–Pb isotope data of zircons of graphite schist from the VOG. Table S4: U–Pb isotope data of zircons of pegmatite veins from the ANG and VOG. Table S5: U–Pb isotope data of zircons of quartz veins from the ANG and VOG. Table S6: Electron microprobe analyses of tourmaline from the ANG.

Author Contributions: M.-J.Y.: data curation, formal analysis, investigation, validation, visualization, writing—original draft; Y.-J.D.: conceptualization, investigation, funding acquisition, project adminis-

tration, validation, supervision, writing–review and editing; D.Z.: conceptualization, investigation, writing–review and editing; D.-T.W.: investigation, writing–review and editing; Y.F.: investigation; X.-M.Z.: investigation, data curation, formal analysis. All authors have read and agreed to the published version of the manuscript.

Funding: This work was supported by the Shenyang Center, China Geological Survey authorized item: Mineral resources potential evaluation project of the Russian Far-East and Madagascar [DD20160104]; Investigation and evaluation of graphite minerals in Madagascar [DD20160104-02]. We appreciate Madagascar Sands Mining Co. LTD, Antananarivo. for their support during fieldwork.

Data Availability Statement: The data from this publication have been summarized in Supplementary Tables S1–S6.

Acknowledgments: This study was supported by the Investigation and evaluation of graphite minerals in Madagascar [DD20160104-02] project. We would like to acknowledge five anonymous reviewers for their constructive reviews of the manuscript.

Conflicts of Interest: The authors declare no competing interests.

References

- Fang, Y.; Wei, F.C. Global graphite resources. *Refract. Lime* **2009**, *34*, 62–63. (In Chinese with English Abstract)
- Gao, T.M.; Chen, Q.S.; Yu, W.J.; Li, S. Projection of China’s graphite demand and development prospects. *Resour. Sci.* **2015**, *37*, 1059–1067. (In Chinese with English Abstract)
- Wang, X.; Hu, L.S.; Xia, L.; Li, J.; Chen, R.Q. Graphite resources and graphite purification methods research. *Chem. Ind. Times* **2015**, *29*, 19–22. (In Chinese with English Abstract)
- Zhang, F.L.; Zhang, S.Y.; Wu, S. Development situation and future prospects of graphite industry in China. *Carbon Tech.* **2015**, *34*, 1–10. (In Chinese with English Abstract)
- Wu, X.H.; Peng, C.Y.; Yuan, P. Research on the current situation and development strategy of Natural graphite industry in foreign countries. *China Nonmet. Miner. Ind.* **2016**, *122*, 10–11. (In Chinese with English Abstract)
- You, G.Y.; Zou, C.X.; Liu, D.; Lin, N.F.; Xu, D.L.; Wu, D.; Xu, M.J.; Shen, W.T. Suggestions on graphite exploitation and environmental protection. *China Popul. Resour. Environ.* **2016**, *26*, 421–423. (In Chinese with English Abstract)
- Zhang, S.J.; Cui, L.W.; Zhang, Y.W.; Han, J.; Shang, L. Summarise on the graphite mineral resources and their distribution at home and abroad. *China Min. Mag.* **2018**, *27*, 8–14. (In Chinese with English Abstract)
- Henne, A.; Craw, D. Synmetamorphic carbon mobility and graphite enrichment in metaturbidites as a precursor to orogenic gold mineralization, Otago Schist, New Zealand. *Miner. Depos* **2012**, *47*, 781–797. [\[CrossRef\]](#)
- Khanchuk, A.I.; Nechaev, V.P.; Plyusnina, L.P.; Berdnikov, N.V.; Molchanov, V.P.; Vysotskiy, S.V. Noble metal-graphite mineralization: A comparative study of the carbonaceous granite-gneiss complex and shales of the Russian Far East. *Ore Geol. Rev.* **2013**, *53*, 276–286. [\[CrossRef\]](#)
- Luque, F.J.; Huizenga, J.M.; Crespo-Feo, E.; Wada, H.; Ortega, L.; Barrenechea, J.F. Vein graphite deposits: Geological settings, origin, and economic significance. *Miner. Depos.* **2014**, *49*, 261–277. [\[CrossRef\]](#)
- Rosing-Schow, N.; Bagas, L.; Kolb, J.; Balic-Zunic, T.; Korte, C.; Fiorentini, M.L. Hydrothermal flake graphite mineralization in Paleoproterozoic rocks of south-east Greenland. *Mineral. Depos* **2017**, *52*, 769–789. [\[CrossRef\]](#)
- Villar, J.E.; Francisco, J.C. Summary of the global graphite market and the prospectives for the spanish deposits. *Bol. Geol. Y Min.* **2019**, *130*, 27–46.
- Ma, J.H.; Liu, Y.; Ma, X.H.; Ti, Y.S.; Ma, Y.W.; Zhao, G.; Zhang, X.N.; Zhang, J.; Li, Y.X.; Zhao, L. Geological Characteristics and Genetic Analysis of Graphite Deposits in Madagascar. *Geol. Explor.* **2020**, *56*, 878–888.
- Huang, G.P.; Hu, Q.Y.; Chen, D.M.; Li, L.; Zhang, Z.; Zhu, A.A.; Xu, H.B. Overview of Madagascar Geology and Minerals. *Resour. Environ. Eng.* **2014**, *28*, 626–632. (In Chinese)
- An, T.; Li, J.W. Analysis of the present supply-demand situation and the trend of global graphite resource. *China Min. Mag.* **2017**, *26*, 11–15. (In Chinese with English Abstract)
- Wang, L.; Fan, J.L.; Feng, Y.W. Graphite Resources Status Quo and Distribution of Graphite Deposits in China. *Coal Geol. China* **2017**, *29*, 5–9. (In Chinese with English Abstract)
- USGS Mineral Commodity Summarise 2022. Available online: <http://minerals.usgs.gov> (accessed on 25 April 2023).
- Li, H.; Hong, T.; Liu, S.K.; Ke, Q.; Yang, Z.Q.; Ma, Y.C.; Wang, X.H.; Niu, L.; Kang, K.; Xu, X.W. Genesis of the Graphite from the Tugeman Graphite Deposit, Xinjiang, China: Evidence for Carbon Isotope Refining by Fluids Associated with the Ductile Shear Zone. *Minerals* **2023**, *13*, 1328. [\[CrossRef\]](#)
- Kumar, M.S. Carbon isotopic composition of graphite in metamorphic rocks from Lützow-Holm Complex, East Antarctica: Implications for carbon geodynamic cycle in continental crust. *J. Mineral. Petrol. Sci.* **2023**, *118*, 230401.
- George, N.D.C.; Karl, S.M.; Regan, S.P.; Johnson, C.A.; Ellison, E.T.; Caine, J.S.; Holm-Denoma, C.S.; Pianowski, L.S.; Marsh, J.H. Insights into the metamorphic history and origin of flake graphite mineralization at the Graphite Creek graphite deposit, Seward Peninsula, Alaska, USA. *Miner. Depos.* **2023**, *58*, 939–962.

21. Nan, J.; Peng, Z.; Wang, C.; Papineau, D.; She, Z.; Guo, Z.; Peng, X.; Tao, R.; Nan, J.; Peng, Z.; et al. Molecular mechanism of metamorphic alteration on traces of early life in banded iron formations. *Earth Planet. Sci. Lett.* **2023**, *615*, 118226. [[CrossRef](#)]
22. Zhu, J.J.; Liu, F.L.; Wang, F.; Xu, W.T.; Liu, F.X.; Shi, C. Carbon isotope and geochemical characteristics of the Paleoproterozoic graphite deposits in the Jiao-Liao-Ji belt, North China Craton: Implications for genesis and depositional environment. *Precambrian Res.* **2021**, *362*, 106320. [[CrossRef](#)]
23. Perry, E.C., Jr.; Ahmad, S.N. Carbon isotope composition of graphite and carbonate minerals from 3.8-AE metamorphosed sediments, Isukasia. *Greenland. Earth Planet. Sci. Lett.* **1977**, *36*, 280–284. [[CrossRef](#)]
24. Wang, J.Y.; Liu, J.C.; Zhang, H.D.; Zhang, H.R.; Li, Y. Metamorphism, geochemistry, and carbon source on sedimentary-metamorphic graphite deposits in eastern Shandong. *China Geol.* **2019**, *55*, 3748–3769. [[CrossRef](#)]
25. Yang, M.J.; Di, Y.J.; Zhang, D.; Wu, D.T.; Fang, Y.; Wang, S.W. Genetic analysis of Antanisoa graphite deposit in Madagascar. *Miner. Depos.* **2020**, *39*, 381–396. (In Chinese with English Abstract)
26. Rumble, D.; Hoering, T.C. Carbon isotope geochemistry of graphite vein deposits from New Hampshire, U.S.A. *Geochim. Cosmochim. Acta* **1986**, *50*, 1239–1247. [[CrossRef](#)]
27. Dissanayake, C.; Chandrajith, R.; Boudou, J. Biogenic graphite as a potential geomarker-application to continental reconstructions of Pan-African Gondwana terrains. *Gondwana Res.* **2000**, *3*, 405–413. [[CrossRef](#)]
28. Papineau, D.; De-Gregorio, B.T.; Stroud, R.M.; Steele, A.; Pecoits, E.; Konhauser, K.; Wang, J.; Fogel, M.L. Ancient graphite in the Eoarchean quartz-pyroxene rocks from Akilia in southern West Greenland II: Isotopic and chemical compositions and comparison with Paleoproterozoic banded iron formations. *Geochim. Cosmochim. Acta* **2010**, *74*, 5884–5905. [[CrossRef](#)]
29. Luque, F.; Crespo-Feo, E.; Barrenechea, J.; Ortega, L. Carbon isotopes of graphite: Implications on fluid history. *Geosci. Front* **2012**, *3*, 197–207. [[CrossRef](#)]
30. Beyssac, O.; Rumble, D. Graphitic carbon: A ubiquitous, diverse, and useful geomaterial. *Elements* **2014**, *10*, 415–420. [[CrossRef](#)]
31. Dienes, P. Stable isotope variations in carbonatite. In *Car-Bonitites: Genesis and Evolution*; Bell, K., Ed.; Unwin Hyman: London, UK, 1989; pp. 301–359.
32. Dienes, P. The carbon isotope geochemistry of mantle xenoliths. *Earth-Sci. Rev.* **2002**, *58*, 247–278. [[CrossRef](#)]
33. Javoy, M.; Pineau, F.; Delorme, H. Carbon and nitrogen isotopes in the mantle. *Chem. Geol.* **1986**, *57*, 41–62. [[CrossRef](#)]
34. Dienes, P.; Stachel, T.; Harris, J.W. Systematic regional variations in diamond carbon isotopic composition and inclusion chemistry beneath the Orapa kimberlite cluster, in Botswana. *Lithos* **2009**, *112*, 776–784. [[CrossRef](#)]
35. Luque, F.J.; Ortega, L.; Barrenechea, J.F.; Millward, D.; Beyssac, O.; Huizenga, J.M. Deposition of highly crystalline graphite from moderate temperature fluids. *Geology* **2009**, *37*, 275–278. [[CrossRef](#)]
36. Touret, J.L.R.; Huizenga, J.M.; Kehelpannala, K.V.W.; Piccoli, F. Vein-type graphite deposits in Sri Lanka: The ultimate fate of granulite fluids. *Chem. Geol.* **2019**, *508*, 167–181. [[CrossRef](#)]
37. Zhu, J.J.; Zhang, L.F.; Tao, R.B.; Fei, Y.W. The formation of graphite-rich eclogite vein in S. W. Tianshan (China) and its implication for deep carbon cycling in subduction zone. *Chem. Geol.* **2020**, *533*, 119430. [[CrossRef](#)]
38. Touzain, P.; Balasooriya, N.; Bandaranayake, K.; Descolas-Gros, C. Vein graphite from the Bogala and Kahatagaha-Kolongaha mines, Sri Lanka: A possible origin. *Can. Mineral.* **2010**, *48*, 1373–1384. [[CrossRef](#)]
39. Zhang, C.; Santosh, M. Coupled laser Raman spectroscopy and carbon stable isotopes of graphite from the khondalite belt of Kerala, southern India (Article). *Lithos* **2019**, *334–335*, 245–253. [[CrossRef](#)]
40. Craig, H. The geochemistry of the stable carbon isotopes. *Geochim. Cosmochim. Acta* **1953**, *3*, 53–92. [[CrossRef](#)]
41. Li, W.H. *Genesis of Vohitasara Graphite Deposit on the East Coast of Madagascar*; China University of Geosciences: Beijing, China, 2018. (In Chinese with English Abstract)
42. Windley, B.F.; Razafiniparany, A.; Razakamanana, T.; Ackermann, D. Tectonic framework of the Precambrian of Madagascar and its Gondwana connections: A review and reappraisal. *Geol. Rundsch.* **1994**, *83*, 642–659. [[CrossRef](#)]
43. Tucker, R.D.; Handke, M.J.; Hamilton, M.A.; Ashwal, L.D.; LeGrange, M.; Rambeloson, R.A. U-Pb geochronology and isotope geochemistry of the Archean granite-greenstone belts of Madagascar. *J. Geol.* **1999**, *107*, 135–153. [[CrossRef](#)]
44. Tucker, R.D.; Roig, J.Y.; Macey, P.H. A new geological framework for south-central Madagascar, and its relevance to the “outof-Africa” hypothesis. *Precambrian Res.* **2011**, *185*, 109–130. [[CrossRef](#)]
45. Tucker, R.D.; Roig, J.Y.; Moine, B.; Delor, C.; Peters, S.G. A geological synthesis of the Precambrian shield in Madagascar. *J. Afr. Earth Sci.* **2014**, *94*, 9–30. [[CrossRef](#)]
46. Goncalves, P.; Nicollet, C.; Lardeaux, J.M. Finite strain pattern in Andriamena unit (north-central Madagascar): Evidence for late Neoproterozoic-Cambrian thrusting during continental convergence. *Precambrian Res.* **2003**, *123*, 135–157. [[CrossRef](#)]
47. Bybee, G.M.; Ashwal, L.D.; Wilson, A.H. New evidence for a volcanic arc on the western margin of a rifting Rodinia from ultramafic intrusions in the Andriamena region, north-central Madagascar. *Earth Planet. Sci. Lett.* **2010**, *293*, 42–53. [[CrossRef](#)]
48. Collins, A.S. Madagascar and the amalgamation of Central Gondwana. *Gondwana Res.* **2006**, *9*, 3–16. [[CrossRef](#)]
49. Macey, P.; Bisnath, A.; Ingram, B.; Yibas, B.; Robson, L.; Adriamanantsoa, E. *Carte Géologique de Madagascar 1:500,000, Feuille N° 5—Maintirano*; Ministère De L’énergie Et Des Mines Projet de Gouvernance des Ressources Minérales: Antananarivo, Madagascar, 2008.
50. Bésairie, H. *Carte Géologique à 1:2,000,000 de Madagascar*; Service Géologique De Madagaskara: Antananarivo, Madagascar, 1973.
51. Vachette, M.; Hottin, G. Age de 1066 M.A. au strontium ajusté’ par isochrone sur roches totales des formations granitoides de Brickaville (est de Madagascar). *Comptes Rendus L’Acadé’Mie Des Sci. Paris* **1977**, *284*, 1135–1138.

52. Vachette, M.; Hottin, G. *The Precambrian of Madagascar through Wholerock Rb/Sr Isochron Data*; Histoire du Gondwana vue de Madagascar: Antananarivo, Madagascar, 1979.
53. Hebei Geological Engineering Exploration Institute. *The No 7–13 Exploration Lines of General Exploration Report in Ambahita Graphite Deposit, National Tullia Province, Madagascar*; Hebei Geological Engineering Exploration Institute: Baoding, China, 2018; pp. 1–89. (In Chinese)
54. Li, X.H.; Liu, Y.; Li, Q.L.; Guo, C.H.; Chamberlain, K.R. Precise determination of Phanerozoic zircon Pb/Pb age by multicollector SIMS without external standardization. *Geochem. Geophys. Geosyst.* **2009**, *10*, Q04010.
55. Compston, W.; Williams, I.S.; Kirschvink, J.L.; Zhang, Z.C.; Ma, G.G. Zircon U-Pb ages for the Early Cambrian time scale. *J. Geol. Soc. Lond.* **1992**, *149*, 171–184. [[CrossRef](#)]
56. Stone, M. Petrogenetic implications from biotite compositional variations in the Cornubian granite batholith. *Mineral. Mag.* **2000**, *64*, 729–735. [[CrossRef](#)]
57. Foster, M.D. *Interpretation of the Composition of Trioctahedral Micas*; United States Geological Survey: Reston, VA, USA, 1960; Volume 354, pp. 1–146.
58. Hoskin, P.W.O.; Schaltegger, U. The composition of zircon and igneous and metamorphic petrogenesis. *Rev. Mineral. Geochem.* **2003**, *53*, 27–62. [[CrossRef](#)]
59. Mitchell, C.J. *Industrial Minerals Laboratory Manual: Flake graphite. British Geological Survey Technical Report*; British Geological Survey: Nottingham, UK, 1993; Volume 92, pp. 30–31.
60. Winchell, A.N. A theory for the origin of graphite as exemplified in the graphite deposit near Dillon, Montana. *Econ. Geol.* **1911**, *6*, 218–230. [[CrossRef](#)]
61. Ortega, L.; Millward, D.; Luque, F.J.; Barrenechea, J.F.; Beyssac, O.; Huizenga, J.M.; Rodas, M.; Clarke, S.M. The graphite deposit at Borrowdale (UK): A catastrophic mineralizing event associated with Ordovician magmatism. *Geochim. Et Cosmochim. Acta* **2010**, *74*, 2429–2449. [[CrossRef](#)]
62. Barrenechea, J.F.; Luque, F.J.; Millward, D.; Ortega, L.; Beyssac, O.; Rodas, M. Graphite morphologies from the Borrowdale deposit (NW England, UK): Raman and SIMS data. *Contrib. Mineral. Petrol.* **2009**, *158*, 37–51. [[CrossRef](#)]
63. Simakin, A.G. Poroelastic response to rapid decarbonisation as a mechanism of the diamonds formation in the mantle wedge of Kamchatka. *Russ. J. Earth Sci.* **2019**, *19*, ES5006. [[CrossRef](#)]
64. Lowenstern, J.B. Carbon dioxide in magmas and implications for hydrothermal systems. *Miner. Depos.* **2001**, *36*, 490–502. [[CrossRef](#)]
65. Shcheka, S.S.; Wiedenbeck, M.; Frost, D.J.; Keppler, H. Carbon solubility in mantle minerals. *Earth Planet. Sci. Lett.* **2006**, *245*, 730–742. [[CrossRef](#)]
66. Doroshkevich, A.G.; Wall, A.F.; Ripp, A.G.S. Magmatic graphite in dolomite carbonatite at Pogranichnoe, NorthTransbaikalia, Russia. *Contrib. Mineral. Petrol.* **2007**, *153*, 339–353. [[CrossRef](#)]
67. Rajesh, V.J.; Arai, S.; Satish-Kumar, M. Origin of graphite in glimmerite and spinellite in Achankovil Shear Zone, southern India. *J. Mineral. Petrol. Sci.* **2009**, *104*, 407–412. [[CrossRef](#)]
68. Palyanov, Y.N.; Borzdov, Y.M.; Bataleva, Y.V.; Sokol, A.G.; Palyanova, G.A.; Kupriyanov, I.N. Reducing role of sulfides and diamond formation in the Earth's mantle. *Earth Planet. Sci. Lett.* **2007**, *260*, 242–256. [[CrossRef](#)]
69. Tucker, R.D.; Kusky, T.M.; Buchwaldt, R.; Handke, M.J. Neoproterozoic nappes and superposed folding of the Itremo Group, west-central Madagascar. *Gondwana Res.* **2007**, *12*, 356–379. [[CrossRef](#)]
70. Nédélec, A.; Ralison, B.; Bouchez, J.L.; Grégoire, V. Structure and metamorphism of the granitic basement around Antananarivo: A key to the Pan-African history of central Madagascar and its Gondwana connections. *Tectonics* **2000**, *19*, 997–1020. [[CrossRef](#)]
71. Tucker, R.D.; Peters, S.G.; Roig, J.Y.; Théveniaut, H.; Delor, C. *Cartes Géologique et Métallogéniques de la République de Madagascar à 1/1000000*; United States Geological Survey: Reston, VA, USA, 2012; pp. 1–257.
72. Henry, D.J.; Guidotti, C.V. Tourmaline as a petrogenetic indicator mineral: An example from the staurolite-grade metapelites of NW Maine. *Am. Miner.* **1985**, *70*, 1–15.
73. Hinsberg, V.J.; Henry, D.J.; Dutrow, B.L. Tourmaline as a Petrologic Forensic Mineral: A Unique Recorder of Its Geologic Past. *Elements* **2011**, *7*, 327–332. [[CrossRef](#)]
74. Slack, J.F.; Trumbull, R.B. Tourmaline as a recorder of ore-forming processes. *Elements* **2011**, *7*, 321–326. [[CrossRef](#)]
75. Deer, W.A.; Howie, R.A.; Zussman, J. *An Introduction to the Rockforming Minerals*, 2nd ed.; Longman scientific and technical; Mineralogical Society of Great Britain and Ireland: London, UK, 1992; pp. 1–696.
76. Zhou, Z.X. The origin of intrusive mass in Fengshandong, Hubei province. *Acta Petrologica Sin.* **1986**, *2*, 59–70. (In Chinese with English Abstract)
77. Pili, E.; Sheppard, S.M.F.; Lardeaux, J.M. Fluid-Rock Interaction in the Granulites of Madagascar and Lithospheric-Scale Transfer of fluids. *Gondwana Res.* **1999**, *2*, 341–350. [[CrossRef](#)]
78. Martelat, J.E.; Vidal, G.; Lardeaux, J.M.; Nicollet, C.; Rakotondrazafy, R. Images spatiales et tectoniques profondes des continents: l'exemple du Sud-Ouest de Madagascar. *C. R. Acad. Sci. Paris* **1995**, *321*, 325–332.
79. Martelat, J.E.; Nicollet, C.; Lardeaux, J.M.; Vidal, G.; Rakotondrazafy, R. Lithospheric tectonic structures developed under high-grade metamorphism in the southern part of Madagascar. *Geodin. Acta* **1997**, *10*, 94–114. [[CrossRef](#)]
80. Pili, E. Distribution and Transfer of Fluids at the Scale of the Lithosphere: Geochemical and Geophysical Investigation of Granulites from Madagascar. Ph.D. Thesis, Université Claude Bernard Lyon, Lyon, France, 1997.

81. Pili, E.; Sheppard, S.M.F.; Lardeaux, J.M.; Martelat, J.E.; Nicollet, C. Fluid flow versus scale of shear zones in the lower continental crust and the granulite paradox. *Geology* **1997**, *25*, 15–18. [[CrossRef](#)]
82. Pili, E.; Ricard, Y.; Lardeaux, J.M.; Sheppard, S.M.F. Lithospheric shear zones and mantle-crust connections. *Tectonophysics* **1997**, *280*, 15–29. [[CrossRef](#)]
83. Zhang, Y.; Zindler, A. Distribution and evolution of carbon and nitrogen in Earth. *Earth Planet. Sci. Lett* **1993**, *117*, 333–345.
84. Martin, R.F.; Randrianandrisana, A.; Boulvais, P. Ampandrandava and similar phlogopite deposits in southern Madagascar: Derivation from a silicocarbonatitic melt of crustal origin. *J. Afr. Earth Sci.* **2014**, *94*, 111–118. [[CrossRef](#)]
85. Ramambazafy, A.; Moine, B.; Rakotondrazafy, M.; Cuney, M. Significance of carbonic fluids in the granulites and skarns of southeast Madagascar. *Earth Planet. Sci.* **1998**, *327*, 743–748.
86. Meert, J.G. A synopsis of events related to the assembly of eastern Gondwana. *Tectonophysics* **2003**, *362*, 1–40. [[CrossRef](#)]
87. Armistead, S.E.; Collins, A.S.; Redaa, A.; Jepson, G.; Gillespie, J.; Gilbert, S.; Blades, M.L.; Foden, J.D.; Razakamanana, T. Structural evolution and medium-temperature thermochronology of central Madagascar: Implications for Gondwana amalgamation. *J. Geol. Soc.* **2020**, *177*, 784–798. [[CrossRef](#)]
88. Paquette, J.L.; Nédélec, A. A new insight into Pan-African tectonics in the east-west Gondwana collision zone by U-Pb zircon dating of granites from central Madagascar. *Earth Planet. Sci. Lett.* **1998**, *155*, 45–56. [[CrossRef](#)]
89. Collins, A.S. The Tectonic Evolution of Madagascar: Its Place in the East African Orogen. *Gondwana Res.* **2000**, *3*, 549–552. [[CrossRef](#)]
90. Kröner, A.; Hegner, E.; Collins, A.S.; Windley, B.F.; Brewer, T.S.; Razakamanana, T.; Pidgeon, R.T. Age and magmatic history of the Antananarivo Block, central Madagascar, as derived from zircon geochronology and Nd isotopic systematics. *Am. J. Sci.* **2000**, *300*, 251–288. [[CrossRef](#)]
91. Collins, A.S.; Fitzsimons, I.C.W.; Hulscher, B.; Razakamanana, T. Structure of the eastern margin of the East African Orogen in central Madagascar. *Precambrian Res.* **2003**, *123*, 111–133. [[CrossRef](#)]
92. Raharimahefa, T.; Kusky, T.M. Temporal evolution of the Angavo and related shear zones in Gondwana: Constraints from LA-MC-ICP-MS U–Pb zircon ages of granitoids and gneiss from central Madagascar. *Precambrian Res.* **2010**, *182*, 30–42. [[CrossRef](#)]
93. Hulscher, B.; Fitzsimons, I.C.W. Sinistral oblique convergence at approximately 550 Ma in central Madagascar; key constraints on the final amalgamation of Gondwanaland. *Geol. Soc. Am.* **2003**, *35*, 345.
94. Andriamarofahatra, J.; Delabois, H.; Nicollet, C. Monazites and zircons U–Pb dating of the last major granulitic tectonometamorphic event in the southeastern part of Madagascar. *Comptes Rendus L Acad. Sci. Ser. II* **1990**, *310*, 1643–1648.
95. Paquette, J.L.; Nédélec, A.; Moine, B.; Rakotondrazafy, M. U–Pb, single zircon Pb–evaporation, and Sm–Nd isotopic study of a granulite domain in SE Madagascar. *J. Geol.* **1994**, *102*, 523–538. [[CrossRef](#)]
96. Kröner, A.; Braun, I.; Jaeckel, P. Zircon geochronology of anatexitic melts and residues from a high-grade pelitic assemblage at Ihosy, southern Madagascar: Evidence for Pan-African granulite metamorphism. *Geol. Mag.* **1996**, *133*, 311–323. [[CrossRef](#)]
97. Nicollet, C.; Montel, J.M.; Foret, S.; Martelat, J.E.; Rakotondrazafy, R.; Lardeaux, J.M. E–Probe monazite dating in Madagascar: A good example of the usefulness of the in-situ dating method. In Proceedings of the UNESCO–IUGS–IGCP–348/368, International Field Workshop on Proterozoic Geology of Madagascar, Antananarivo, Madagascar, 16–30 August 1997; Volume 348, pp. 65–66.
98. Markl, G.; Bäuerle, J.; Grujic, D. Metamorphic evolution of Pan-African granulite facies metapelites from southern Madagascar. *Precambrian Res.* **2000**, *102*, 47–68. [[CrossRef](#)]
99. Jöns, N.; Schenk, V. The ultrahigh temperature granulites of southern Madagascar in a polymetamorphic context: Implications for the amalgamation of the Gondwana supercontinent. *Eur. J. Mineral.* **2011**, *23*, 127–156.
100. Collins, A.S. Depositional age, provenance and metamorphic age of metasedimentary rocks from southern Madagascar. *Gondwana Res.* **2012**, *21*, 353–361. [[CrossRef](#)]
101. Rakotondrazafy, R.; Pierdzig, S.; Raith, M.M.; Hoernes, S. Phlogopite mineralisations in the Beraketa belt of southern Madagascar: A spectacular example of channelized fluid flow and fluid–rock interaction. In Proceedings of the UNESCO–IUGS–IGCP International Field Workshop on the Proterozoic Geology of Madagascar, Antananarivo, Madagascar, 16–30 August 1997; p. 81.

Disclaimer/Publisher’s Note: The statements, opinions and data contained in all publications are solely those of the individual author(s) and contributor(s) and not of MDPI and/or the editor(s). MDPI and/or the editor(s) disclaim responsibility for any injury to people or property resulting from any ideas, methods, instructions or products referred to in the content.